Environmental
Science
Nano

ROYAL SOCIETY
OF CHEMISTRY

PAPER

View Article Online
View Journal | View Issue

Check for updates

Cite this: *Environ. Sci.: Nano*, 2026, **13**, 1004

Atomic-scale structure of gadolinium in nanocrystalline fluorapatite from marine sediments

Alain Manceau, *[ab] Andrea Giacomelli, [b] Yan Li, [a] Anne-Claire Gaillot, [c] Jianlin Liao, [a] Lorenzo Spadini,[d] Alexandre Simionovici, [e] Andrea Koschinsky, [f] Olivier Mathon[a] and Stephan N. Steinmann *[b]

Received 14th November 2025,
Accepted 15th January 2026

DOI: 10.1039/d5en01056j

rsc.li/es-nano

Deep-sea sediments hold large quantities of critical rare earth-elements and yttrium (REY) sequestered in nanoparticulate biogenic fluorapatite ($Ca_5(CO_3)_x(PO_4)_{3-x}F_{1+x}$). Understanding their enrichment processes and improving recovery and mineral processing methods require atomic-scale information about their chemical form, but it is difficult to obtain. Here, we use novel high-energy-resolution fluorescence-detected extended X-ray absorption fine structure (HERFD-EXAFS) spectroscopy to elucidate the local structure of gadolinium (Gd) in the highly enriched REY deposit from the Clarion–Clipperton fracture zone (CCFZ) in the Pacific Ocean. Our findings reveal that Gd is neither incorporated into the apatite structure nor precipitated alongside Ce in a Ce–PO_4 precipitate. Instead, it is bound at short-range distances to Ca and PO_4 in a defective apatite-type bonding environment within an amorphous matrix that encases fluorapatite nanocrystals. Density functional theory (DFT) suggests that Gd and Y, whose atomic fraction is ten times higher than that of Gd, are not dispersed throughout the amorphous matrix, but are likely segregated at medium-range distances. The entrapment of Ce, Gd, and Y within an amorphous matrix explains, at the microscopic level, why REY can be easily recovered through straightforward acid leaching. This is due to the intrinsic instability of disordered atomic structures compared to crystalline phases. This research highlights the complementarity of HERFD-EXAFS and DFT calculations for atomic-scale analysis of trace elements in complex natural matrices. It establishes a basis for their use across diverse terrestrial and marine materials.

Environmental significance

A long-accepted view is that REY are contained inside the structure of fluorapatite (FAp) in marine sediments. We question this view and show that Gd, hosted in biogenic FAp from the Clarion Clipperton fracture zone in the Pacific Ocean, is bound to calcium and phosphate within a defective apatite-like structure, located inside an amorphous matrix surrounding FAp nanocrystals. In practical terms, selective leaching protocols for extracting REY from REY-rich sediments could target the coating while leaving the crystal core, which is relatively resistant to dissolution, largely intact, potentially reducing reagent use and limiting co-dissolution of Ca and P from the FAp lattice.

1. Introduction

Situated in the middle of the lanthanide 4f series, gadolinium (Gd) displays several notable physical characteristics that drive its use in various scientific and technological fields, such as medical imaging, nuclear physics, data storage, and advanced materials. In its fundamental state ([Xe] $4f^7$), the trivalent Gd^{3+} ion possesses seven 4f electrons with all spins aligned, resulting in the highest total spin possible for a mononuclear metal ion (S = 7/2). The large spin magnetic moment of Gd is extensively utilized in magnetic resonance imaging (MRI), where Gd is employed as a contrast agent.[1] Additionally, its magnetic properties, combined with a Curie point close to room temperature for both Gd and several of its alloys and salts, enable room-temperature magnetic refrigeration.[2] Furthermore, the ^{155}Gd and ^{157}Gd isotopes exhibit high neutron capture cross sections, which are applied in nuclear technology for

---

[a] *European Synchrotron Radiation Facility (ESRF), 38043 Grenoble, France. E-mail: alain.manceau@esrf.fr*

[b] *ENS de Lyon, CNRS, Laboratoire de Chimie, 69342 Lyon, France. E-mail: alain.manceau@ens-lyon.fr*

[c] *Nantes Université, CNRS, Institut des Matériaux de Nantes Jean Rouxel, IMN, 44000 Nantes, France*

[d] *Université Grenoble Alpes, CNRS, Institut des Géosciences de l'Environnement, 38000 Grenoble, France*

[e] *Université Grenoble Alpes, CNRS, ISTerre, 38000 Grenoble, France*

[f] *School of Science, Department of Physics and Earth Sciences, Constructor University, D-28759 Bremen, Germany*

reactor control rods[3] and in engineering for neutron shielding.[4,5]

The majority of global Gd production originates from ion-adsorption clays that form on land as rare-earth elements and yttrium (REY) leach from granitic rocks and are then adsorbed by clays in the weathered surface crust.[6–10] Deep-sea muds, found in pelagic basins, are rich in valuable heavy REY, including Gd. Kato *et al.* (2011)[11] showed that over 90% of the total REY in bulk sediments can be efficiently recovered with simple acid leaching (*e.g.*, 0.5 M HCl for 3 h at 25 °C), indicating the potential of deep-sea sediments as a resource for REY. The ease of extraction initially suggested that REY are contained within the clay portion of the sediment, akin to terrestrial sources. However, later research revealed that the REY are mainly associated with carbonate fluorapatite (CFA, $Ca_5(CO_3)_x(PO_4)_{3-x}F_{1+x}$).[12–23] There are two types of CFA, one formed through chemical precipitation (authigenic CFA),[23–25] and the other originating from the remnants of marine fauna (*e.g.*, fish bones and teeth, biogenic CFA).[13,17–19,21,26–29] The prevailing view had been that REY are incorporated into the structure of CFA. Nevertheless, this hypothesis does not align with the ease of REY extraction from marine deposits, as fluorapatite has slow solubility kinetics,[30,31] even at low pH.[32]

Recent studies using extended X-ray absorption fine structure (EXAFS) spectroscopy and electron microscopy have shown that cerium (Ce)[33] and yttrium (Y)[34] are incorporated into an amorphous Ca–phosphate matrix surrounding CFA nanocrystals (Fig. 1). The REY within this phase are more susceptible to leaching, because amorphous phases have a less ordered atomic structure than crystalline phases. Ce (Z = 58) and Y (Z = 39) are not bound together in the amorphous matrix embedding the CFA grains. Ce occurs as Ce–phosphate ($CePO_4$) clusters,[33] whereas Y is mononuclear at short-range distances and bonded to CaO_6 octahedra and PO_4 groups in a disordered apatite-type structure.[34]

This study investigates the incorporation of Gd (Z = 64) in biogenic CFA. Gd was selected not only for its economic significance but also for its unique electronic properties and mid-range position among lanthanides. Both Ce and Gd have similar concentrations in CFA (2000 mg kg^{-1} *vs.* 1500 mg kg^{-1}, respectively), while the molar abundance of Y is 10 times higher (8500 mg kg^{-1}, $(Y/Gd)_{at}$ = 10.0).[21] This raises questions about the crystal chemistry of Gd in CFA: (1) is it incorporated into the bulk crystal structure or (2) is it precipitated as a phosphate, either with or without Ce or Y ($GdPO_4$, $(Gd,Ce)PO_4$, $(Gd,Y)PO_4$ structures),[35] in the amorphous matrix surrounding the CFA nanocrystals. Because the Y/Gd atomic ratio is about 10, if Gd–Y clusters exist, they might not be detectable at the Y absorption edge using EXAFS,[34] but should be observed at the Gd edge.

In this study, two biogenic CFAs from the Clarion–Clipperton fracture zone (CCFZ) in the Pacific Ocean were collected at 1.94 m (16GC-194, [Gd] = 1548 mg kg^{-1}) and 4.70 m (16GC-470, [Gd] = 1756 mg kg^{-1}) below the seafloor. They were analyzed using the high-energy-resolution fluorescence-detected (HERFD) EXAFS measurement mode.[36] HERFD-

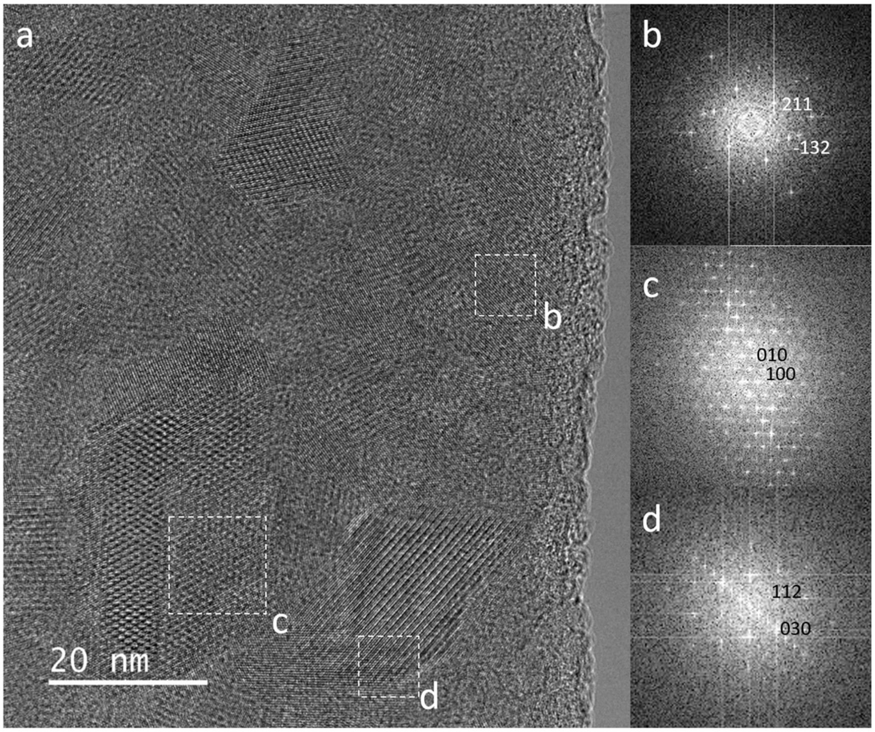

Fig. 1 (a) High-resolution transmission electron microscopy image of bioapatite nanocrystals (16GC-194) embedded in an amorphous matrix. (b–d) FFT patterns of individual bioapatite nanocrystals oriented along the [15-7], [001] and [20-1] zone axes.

EXAFS effectively removes parasitic absorption edges from other REY, which would restrict the energy range of the Gd L_3-edge EXAFS signal. This advanced technique has proven valuable for extracting structural information from multi-elemental materials.[33,34,37–43] EXAFS analysis was complemented with periodic density functional theory (p-DFT) to evaluate the likelihood of Gd forming polynuclear Gd–Gd and Gd–Y clusters.

2. Results and discussion

2.1. EXAFS analysis

2.1.1. References. Fig. 2a compares the Gd EXAFS spectra and radial structure functions (RSF), obtained by Fourier transformation (FT) of the EXAFS spectra, for two references: $GdPO_4 \cdot H_2O$ and a magmatic fluorapatite (m-FAp). DFT2FEFFIT[44] calculation indicates that Gd replaces Ca in

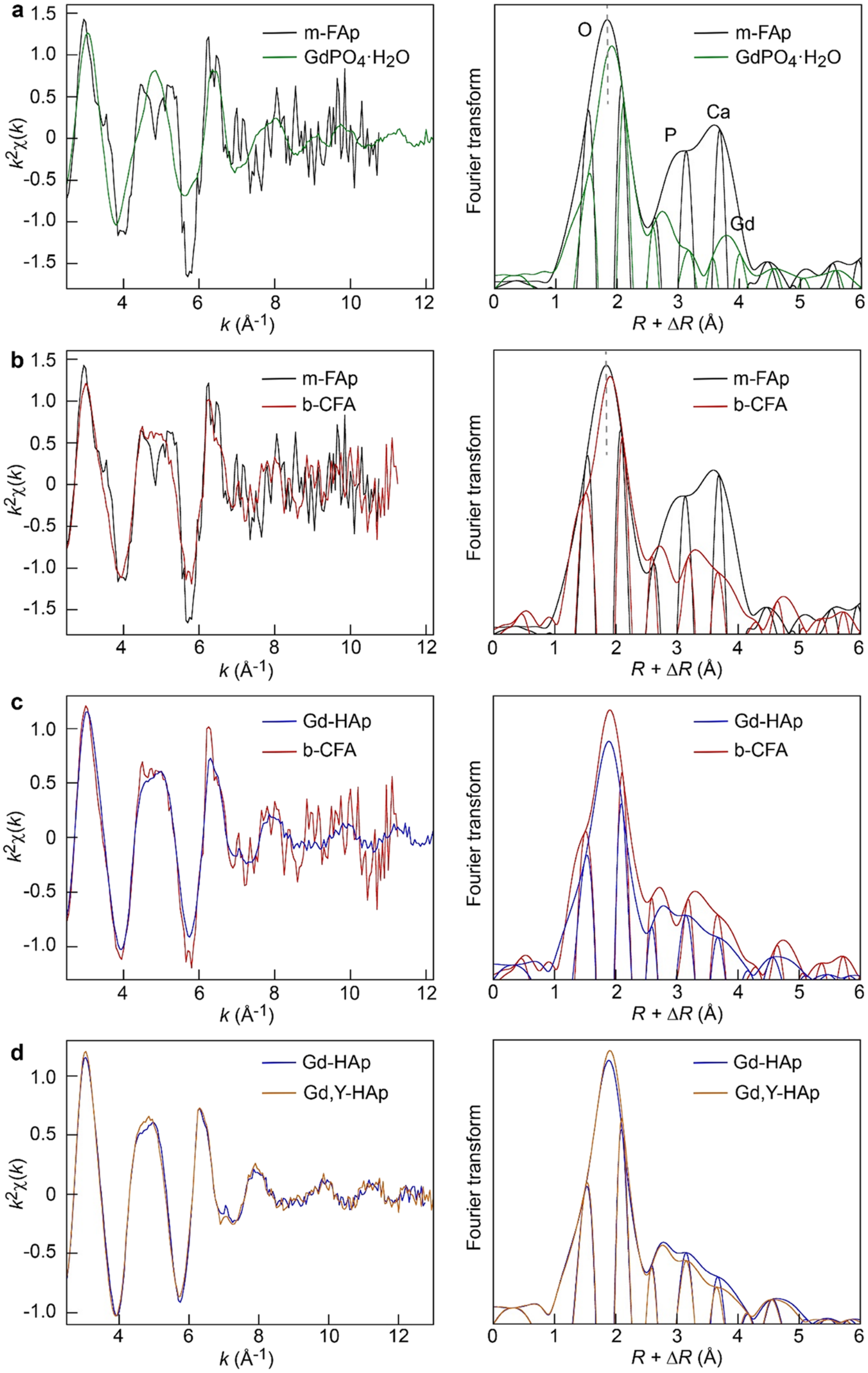

Fig. 2 Gd L_3-edge EXAFS spectra (left) and modulus and imaginary parts of the Fourier transforms (right) for biogenic CFA and references. a) Magmatic FAp from Imilchil (Morocco) and $GdPO_4 \cdot H_2O$. b) Magmatic FAp and biogenic CFA. c) Biogenic CFA and Gd-sorbed hydroxyapatite. d) Gd-sorbed and Gd,Y-sorbed hydroxyapatite.

the Ca(2) site of m-FAp, as predicted by p-DFT[45] (Fig. 3 and S1). The best fit for the $GdPO_4{\cdot}H_2O$ spectrum included two O subshells at 2.34 Å and 2.46 Å (weighted average $\langle d(\text{Gd–O})\rangle$ = 2.40 Å), two P shells at 3.11 Å and 3.70 Å, and a Gd shell at 4.02 Å, aligning with a previous analysis[46] (Fig. S2a, Table 1). For m-FAp, the optimal model involves one O shell at 2.33 Å, two P shells at 3.14 Å and 3.61 Å, and one Ca shell at 4.06 Å, which matches the FAp crystal structure[47] (Fig. S2b, Table 1). The increased Gd–O bond distance in $GdPO_4{\cdot}H_2O$ compared to m-FAp is evident in the FT, where the first peak's modulus and imaginary part are shifted to higher $R + \Delta R$ values (Fig. 2a). The Gd–Gd and Gd–Ca pairs are closely positioned on the FTs ($R + \Delta R$ = 3.7–3.8 Å), due to their similar distances; however, their imaginary parts are offset by approximately $\pi/4$. Fig. 4a illustrates that Gd and Ca exhibit differing backscattering phase shifts. $\varphi_{\text{Ca}}(k)$ decreases nearly linearly with increasing k, while $\varphi_{\text{Gd}}(k)$ displays a complex pattern with two maxima and a valley at k = 6 $Å^{-1}$.[48] This phase contrast accounts for the offset of the imaginary parts for the Gd–Ca and Gd–Gd pairs in the FTs (Fig. 2a), and can be used to distinguish Ca from Gd in CFA.

Table 1 EXAFS fit parameters of the Gd L_3-edge spectra

Sample	Path	N	R (Å)	σ^2 (Å^2)	ΔE (eV)
m-FAp	Gd–O	6.0^a	2.33	0.006	−1.8
	Gd–P1	2.0^a	3.14	0.006^b	
	Gd–P2	3.0^a	3.61	0.006^b	
	Gd–Ca	10^a	4.06	0.009	
$GdPO_4{\cdot}H_2O$	Gd–O1	4.3^c	2.34	0.007^b	0.6
	Gd–O2	3.7^c	2.46	0.007^b	
	Gd–P1	2.0^a	3.11	0.006^b	
	Gd–P2	1.7	3.70	0.006^b	
	Gd–Ca	3.0	4.02	0.010	
Gd-HAp	Gd–O1	5.0^c	2.33	0.009^b	−0.5
	Gd–O2	3.0^c	2.45	0.009^b	
	Gd–P1	2.0^a	3.10	0.008^b	
	Gd–P2	2.1	3.67	0.008^b	
	Gd–Ca	2.7	4.08	0.010^a	
Gd,Y-HAp	Gd–O1	3.7^c	2.32	0.009^b	−1.0
	Gd–O2	4.3^c	2.42	0.009^b	
	Gd–P1	2.0^a	3.10	0.008^b	
	Gd–P2	1.8	3.66	0.008^b	
	Gd–Ca	2.1	4.07	0.010^a	
b-CFA Gd–Ca model	Gd–O	8.0^a	2.37	0.011	−0.9
	Gd–P1	2.0^a	3.10	0.004^b	
	Gd–P2	1.7	3.69	0.004^b	
	Gd–Ca	4.0	4.07	0.010^a	
b-CFA Gd–Y model	Gd–O	8.0^a	2.37	0.011	−0.9
	Gd–P1	2.0^a	3.10	0.004^b	
	Gd–P2	2.8	3.66	0.004^b	
	Gd–Ca	4.5	3.86	0.010^a	

[a] Fixed value. [b] Parameters constrained to suppress correlations between σ and CN. [c] Sum fixed to 8. Accuracy: R = 0.02 Å, CN = 20%.

2.1.2. **Biogenic CFA.** The Gd EXAFS spectra for the two biogenic CFAs are statistically indistinguishable, indicating that the local structural environments around the Gd atoms are similar (Fig. S3). Consequently, the two spectra were averaged for EXAFS fitting and further comparisons to generate a single, higher-quality spectrum (b-CFA). A comparison of the FT for b-CFA and m-FAp shows that Gd has longer Gd–O bond distances in b-CFA, alongside comparable P and Ca atomic shells in both apatites (Fig. 2b). EXAFS fitting of b-CFA identified one O shell at 2.37 Å (σ = 0.10 Å), two P shells at 3.10 Å and 3.69 Å, and one Ca shell at 4.07 Å (Fig. S2c, Table 1). The experimental resolution in distance for the b-CFA data ($\delta R = \pi/(2k_{\max}) = \pi/(2 \times 11.25)$ = 0.14 Å)[49] was insufficient for attempting to fit its EXAFS spectrum with two O subshells. Nevertheless, the fitting results indicate that the O shell has a relatively high disorder parameter (σ = 0.11 Å), suggesting O splitting, similar to observations for $GdPO_4{\cdot}H_2O$ (2.46 Å − 2.34 Å = 0.12 Å). The Gd–Ca shell of b-CFA contains fewer Ca atoms (N = 4.0, Table 1) compared to m-FAp (N = 10), indicated by the diminished amplitude of the Gd–Ca peak at $R + \Delta R$ = 3.7 Å on the RSF (Fig. 2b). This difference, along with the difference in Gd–O bond lengths of 2.37–2.33 = 0.04 Å between the two apatites, indicates that Gd is not incorporated into the crystalline core of the b-CFA structure.

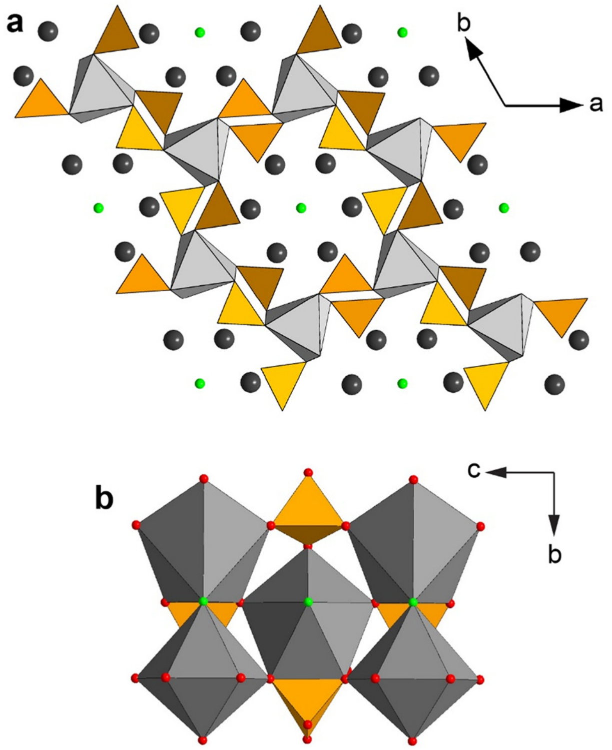

Fig. 3 Structure of FAp. a) Projection along the c direction. The F atom is located in the middle of the tunnels, and the Ca(2) and P atoms are exposed to the lumen of the tunnels and to the mineral surface. b) Polyhedral representation of the local structure of the Ca(2) site projected along the a direction. The Ca_{6+1} polyhedra are connected through corners, and they share one edge and four corners (three are represented) with PO_4 groups. Ca(1) site, light gray; Ca(2) site, dark gray; P, light brown; O, red; F, light green.

2.1.3. **Gd adsorption on HAp.** Since Gd is absent from the CFA structure, it might reside at the mineral surface. This hypothesis was examined using an inner-sphere sorption complex on synthetic hydroxyapatite (Gd-HAp). Fig. 2c

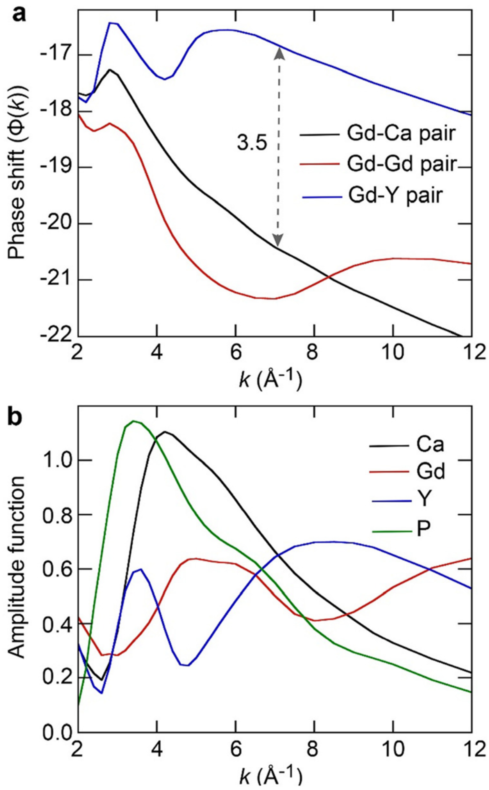

Fig. 4 Graphs of the phase shift functions and scattering amplitudes in the EXAFS function for the Gd–Ca, Gd–Gd, and Gd–Y pairs. a) Phase shift functions. b) Scattering amplitudes.

compares the EXAFS and FTs of b-CFA and Gd-HAp. Their FTs are similar, primarily differing in the higher amplitude of the Gd–P and Gd–Ca peaks for b-CFA. The EXAFS spectrum for Gd-HAp was best fit with one subshell at $d(\text{Gd–O}_1)$ = 2.33 Å and another at $d(\text{Gd–O}_2)$ = 2.45 Å ($\langle d(\text{Gd–O})\rangle$ = 2.375 Å), two P shells at 3.10 Å and 3.67 Å, along with one Ca shell at 4.08 Å (Fig. S2d, Table 1). The resolution in distance for this synthetic reference is $\delta R = \pi/(2 \times 12.75) = 0.12$ Å, which is sufficient for distinguishing the two O subshells. The Ca shell of Gd-HAp consists of N = 2.7 atoms compared to 4.0 for b-CFA, suggesting that Gd is not sorbed either as an inner-sphere surface complex in b-CFA (Table 1).

The difference in N_{Ca} between Gd-HAp and b-CFA aligns with our prior research on yttrium, which showed that Y resides in the amorphous matrix surrounding the CFA nanocrystals (Fig. 1). In the Y-sorbed HAp reference, Y had 1.6 Ca neighbors at 4.03 Å and 2.6 Ca neighbors at 4.11 Å (Table 3 in ref. 34). This suggests that Gd is likely also located within this external amorphous matrix. This raises the question of whether Gd is locally associated with Y, considering that the amorphous matrix hosts ten times more Y atoms than Gd.[21]

2.1.4. Gd and Y co-adsorption on HAp. This inquiry was addressed by co-adsorbing Gd and Y on HAp in a Y/Gd atomic ratio of 10. Fig. 2d shows that Gd-HAp and Gd,Y-HAp have quite similar EXAFS spectra, which at first glance suggests that Gd and Y do not form polynuclear clusters. However, a more detailed analysis reveals that the EXAFS results are ambiguous because the Gd–Ca and Gd–Y photoelectron waves are approximately out-of-phase ($\varphi_{\text{Y}}(k) - \varphi_{\text{Ca}}(k) \approx \pi$, Fig. 4a). Adjusting the Gd–Y distance can counterbalance the phase shift in the fitting. A mathematical solution analogous to the Gd–Ca model was obtained with 4.5 Y atoms at 3.86 Å and 2.8 P at 3.66 Å, in contrast to 4.0 Ca at 4.07 Å and 1.7 P at 3.69 Å for the Gd–Ca model (Fig. S2e, Table 1). The Gd–Y photoelectron wave aligns in phase with the Gd–Ca wave at $k = \pi/[2 \times (4.07\text{–}3.86)] = 7.5$ Å^{-1}, which corresponds to the maximum backscattering amplitude of Y (Fig. 4b). However, the Gd–Y wave amplitude reaches a minimum at k = 4.8 Å^{-1}, requiring compensation in the fitting process. This minimum was balanced by increasing N_{P} from 1.7 in the Gd–Ca model to 2.8 in the Gd–Y model. Gd–Y pairs can also be incorporated into the fit by raising N_{Ca} above 4.0 since $\varphi_{\text{Y}}(k) - \varphi_{\text{Ca}}(k) = \pi$. For instance, a satisfactory fit can also be obtained by setting N_{Ca} = 6.0 and N_{Y} = 2.0. However, the numerical convergence is unstable, necessitating fixed coordination numbers during the least-squares minimization.

Based on these considerations, the Gd–Ca and Gd–Y models are mathematically indistinct. While $d(\text{Gd–Ca})$ = 4.07 Å aligns well with a Gd–PO_4 structure, $d(\text{Gd–Y})$ = 3.86 Å does not. Non-periodic DFT (np-DFT) calculations indicate that $d(\text{Gd–Y})$ = 3.68 Å for an edge-sharing linkage between the Gd and Y polyhedra, and $d(\text{Gd–Y}) > 4.0$ Å for a corner-sharing linkage (Fig. 5). Additionally, as discussed in the p-DFT section below, the formation of Gd–Y pairs at such short distances is thermodynamically disfavored. In summary, our EXAFS analysis of b-CFA indicates that Gd is bonded to phosphates and Ca in the amorphous matrix surrounding the CFA nanocrystals. The next section will discuss the coordination of Gd and its local structure.

2.2. Coordination of Gd

EXAFS has an inherent error of ±1 regarding the number of scatterers (N), which renders the determination of absolute coordination number (CN) inaccurate. An alternative is to use interatomic distances, which typically have errors of ±0.02 Å, well within the variations in distance resulting from the addition or subtraction of an O ligand. The variation of $d(\text{Gd–O})$ with CN was determined based on the structure of the Gd–PO_4 compounds in the inorganic crystal structure database (ICSD). Gd exhibits CN = 6, 7, 8, or 9. Only one compound was found for each CN = 6, 7, and 9, and 9 entries for CN = 8. The Gd–O distances are $d(\text{Gd–O}_6)$ = 2.28 Å, $d(\text{Gd–O}_7)$ = 2.35 Å, $d(\text{Gd–O}_8)$ = 2.37–2.42 Å, and $d(\text{Gd–O}_9)$ = 2.475 Å. The EXAFS distance of 2.40 Å for $GdPO_4 \cdot H_2O$ is consistent with an 8-fold coordination, in agreement with its crystal structure.[46] The EXAFS distance of 2.33 Å for m-FAp is longer than that of the CN = 6 compound (2.28 Å, $Gd(PO_3)_3$),[50] which consists of single GdO_6 octahedra linked by corner-sharing PO_4 groups. In contrast, a good match between experiment and theory is obtained with the p-DFT $\langle d(\text{Gd–O})\rangle$ distance of 2.325 Å for Gd substituted for Ca in the (6 + 1)-fold Ca(2) site of FAp.[45]

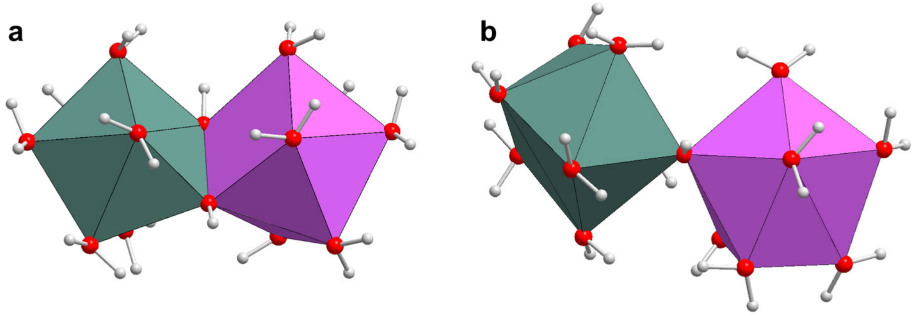

Fig. 5 Edge-sharing (a) and corner-sharing (b) linkages between Gd and Y polyhedra. a) $^{8}Gd(H_2O)_6$–2OH–$^{8}Y(H_2O)_6$ complex. b) $^{8}Gd(H_2O)_7$–OH–$^{8}Y(H_2O)_7$ complex. Non-periodic DFT (np-DFT) calculation (ORCA 5.0.3, PBE0/def2-TZVP).[77] Gd, purple; Y, light green; O, red; H, light gray.

We conclude that d(Gd–O) = 2.37 Å for b-CFA and ⟨d(Gd–O)⟩ = 2.375 Å for Gd-HAp characterize an 8-fold coordination. If one retains an accuracy of ±0.02 Å in EXAFS distances, then both 2.37 Å and 2.375 Å metric parameters are also compatible with a 7-fold coordination. Nonetheless, an 8-fold coordination is more likely, as it is prevalent in Gd–PO_4 structures. The O shell splitting in Gd-HAp can be attributed to water molecules that may deprotonate to OH^- after Gd sorption on HAp crystal surfaces.[51] The apatite surface structure corroborates this view, as it contains two structured water layers H-bonded to the mineral surface.[52] Gd may also include H_2O/OH^- ligands in b-CFA, as EXAFS suggests a splitting in the Gd–O bond distances (σ = 0.11 Å). Gd likely occupies the Ca(2) site in Gd-HAp, since high-resolution reflectivity measurements of the {100} surface structure of FAp showed that this site is exposed to the mineral surface and is deficient in Ca(2) and/or F atoms.[52]

2.3. Connectivity of the GdO_8 polyhedra

The polyhedral configuration of Gd in b-CFA and Gd-HAp can be evaluated using the EXAFS distances, as interatomic distances are shorter when polyhedra share two O ligands (edge linkage) rather than one (corner or vertex linkage). In the nine GdO_8–PO_4 crystal structures from the ICSD, $d(\text{Gd–P})_{\text{edge}}$ varies from 3.06 Å to 3.18 Å, $d(\text{Gd–P})_{\text{corner}}$ ranges from 3.58 Å to 3.89 Å, and $d(\text{Gd–Gd})_{\text{edge}}$ spans from 3.80 Å to 4.04 Å. There is no $d(\text{Gd–Gd})_{\text{corner}}$ connection, and the separation between the GdO_8 polyhedra linked by PO_4 groups exceeds 5.1 Å. Given that a (Gd,Ca)–PO_4 compound does not exist, the Gd–(P,Ca) distances for edge and corner linkages were derived from the Gd(2)-substituted FAp structure calculated by Dahbi *et al.* (2025)[45] using p-DFT. The Ca(2) site in FAp exhibits a 6 + 1 coordination, where the seven vertices of the $Ca(O,F)_{6+1}$ polyhedron are shared with an edge-linked PO_4 group at 3.07 Å, four corner-linked PO_4 groups at 3.26–3.68 Å, and 10 corner-linked $Ca(O,F)_{6+1}$ polyhedra at 3.96–4.14 Å (Fig. 3).[47] The Gd–(P,Ca) distances determined from the np-DFT model are $d(\text{Gd–P})_{\text{edge}}$ = 3.05 Å, $d(\text{Gd–P})_{\text{corner}}$ = 3.18–3.67 Å, and $d(\text{Gd–Ca})_{\text{corner}}$ = 4.00–4.19 Å.

Based on the aforementioned polyhedral considerations, we can now assign the Gd–(P,Ca) EXAFS distances of b-CFA and Gd-HAp to a specific linkage type. d(Gd–P1) = 3.10 Å is attributed to edge sharing and d(Gd–P2) = 3.66–3.67 Å corresponds to corner sharing between GdO_8 and PO_4 (GdO_6–O_2–PO_2 and GdO_7–O–PO_3 linkages, respectively). d(Gd–Ca) = 4.07–4.08 Å is associated with corner sharing between GdO_8 and CaO_6 (GdO_7–O–CaO_5 linkage). Consequently, Gd has the same polyhedral connectivity as Ca(2) in FAp at the local scale (Fig. 3).

2.4. Evaluation of Gd–Gd and Gd–Y pairs from p-DFT

Although Gd–Gd and Gd–Y pairs were excluded from EXAFS analysis, further insight into the thermodynamic stability of Gd–REY pairs was gained through p-DFT. To this end, several atomic configurations and compositions were tested. All geometrically optimized structures are available in the online NOMAD repository. The Gd(2)–FAp structures and computational parameters from our previous work on the incorporation of REY in FAp[45] served as a basis to calculate the stability of the Gd(2)–Gd(2) and Gd(2)–Y(2) pairs. This was accomplished by calculating the energy of the following chemical reactions.

$$\begin{aligned}&\text{GdCcCa}_{79}(\text{PO}_4)_{48}\text{F}_{16} + \text{GdCcCa}_{79}(\text{PO}_4)_{48}\text{F}_{16}\\ &\quad\rightarrow \text{Gd}_2\text{Cc}_2\text{Ca}_{78}(\text{PO}_4)_{48}\text{F}_{16} + \text{Ca}_{80}(\text{PO}_4)_{48}\text{F}_{16}\end{aligned} \tag{1}$$

$$\begin{aligned}&\text{GdCcCa}_{79}(\text{PO}_4)_{48}\text{F}_{16} + \text{YCcCa}_{79}(\text{PO}_4)_{48}\text{F}_{16}\\ &\quad\rightarrow \text{GdYCc}_2\text{Ca}_{78}(\text{PO}_4)_{48}\text{F}_{16} + \text{Ca}_{80}(\text{PO}_4)_{48}\text{F}_{16}\end{aligned} \tag{2}$$

The reaction products include the pure cell and the homo-REY (*i.e.*, Gd–Gd, eqn (1)) or the hetero-REY (*i.e.*, Gd–Y, eqn (2)) enriched structures, while the reactants are the singly Gd- or Y-substituted cells. Carbonates (CO_3^{2-}) in the b-CFA structure were not considered, as we previously showed that they do not link to Y,[34] and we assumed this also applies to Gd. Because the substitution of $(Gd,Y)^{3+}$ for Ca^{2+} is heterovalent, incorporation of REY in FAp requires charge compensation (Cc in eqn (1) and (2)). Two substitutional mechanisms were considered: Na^+ for Ca^{2+} (Cc = Na_1Ca_{-1}) and Si^{4+} for P^{5+} (Cc = $(SiO_4)_1(PO_4)_{-1}$). Na was substituted for Ca(1), which is the preferred site for Na.[45,53]

Table 2 Enrichment energies for eqn (1) and (2)

Substitution pattern	Energy (eV)
2.50% Gd enrichment. Eqn (1)	
Cc: $P^{5+} \rightarrow Si^{4+}$	−0.121
Cc: $Ca^{2+} \rightarrow Na^{+}$	−0.071
1.25% Gd + 1.25% Y enrichment. Eqn (2)	
Cc: $P^{5+} \rightarrow Si^{4+}$	−0.128
Cc: $Ca^{2+} \rightarrow Na^{+}$	−0.101

The reaction energies for the most stable 2Gd and Gd + Y arrangements identified are consistently negative (Table 2). A negative reaction energy indicates that incorporating REY into the same crystal structure is energetically favorable, promoting the enrichment process. The energy gain is most important in the case of Si^{4+} for P^{5+} Cc with −0.128 eV for the Gd + Y hetero-substitution and −0.121 eV for the 2Gd homo-substitution. The Na for Ca Cc is slightly less favorable, with −0.071 eV for Gd + Y and −0.101 eV for 2Gd.

The energy gain also varies with the REY–REY distance separation. There is no linear relationship between ΔE and d(Gd–Gd,Y) within the 4–12 Å distance range examined (Fig. S4–S6). However, the lowest energy structures were consistently found for d(Gd–Gd,Y) = 6.1–6.3 Å for the two atomic pairs and Cc mechanisms. In this configuration, the Gd–Gd and Gd–Y pairs are bridged by a SiO_4/PO_4 tetrahedron (GdO_4–O_2–P/SiO–O–Gd/YO_5 linkage) (Fig. 6). Thus, Gd and Y tend to cluster within the FAp structure, without being directly connected through oxygens (*i.e.*, corner-sharing linkage). An ICSD search shows that $GdO_{6,7}$–$O_{1,2}$–$PO_{1,2}$–O–GdO_7 and $YO_{6,7}$–$O_{1,2}$–$PO_{1,2}$–O–GdO_7 linkages are common in GdO_8–PO_4 and YO_8–PO_4 crystal structures.[54–63] Therefore, the lowest energy Gd–(Gd,Y) linkages in FAp identified by DFT resemble those found in pure GdO_8–PO_4 and YO_8–PO_4 compounds. The predicted clustering of the Gd–Gd and Gd–Y pairs at medium-range distances in FAp is compatible with experimental data, as EXAFS is a local probe sensitive to distances within 4–5 Å.

3. Concluding remarks

Our study on Gd localization in biogenic CFA led us to dismiss its incorporation into the crystal structure, contrary to earlier hypotheses. p-DFT calculations predict that REY strongly prefer the (6 + 1)-fold Ca(2) site over the Ca(1) site in FAp,[45] which we confirmed with EXAFS measurement of a magmatic FAp combined with DFT2FEFFIT calculation. Gd exhibits the same local structure in CFA as Ca(2) in FAp regarding the GdO_8–PO_4 and GdO_8–CaO_6 polyhedral connectivity ($GdO_{6,7}$–$O_{1,2}$–$PO_{2,3}$ and GdO_7–O–CaO_5 linkages, Fig. 3b). However, it has fewer Gd–P and Gd–Ca pairs and is notably 8-fold coordinated to O ligands, some of which are likely H_2O molecules or OH^- groups. The formation of a Gd inner-sphere complex on the surface of the CFA nanocrystals is inconsistent with the number of Ca neighbors, which is 50% higher than in the Gd-sorbed apatite reference (Gd-HAp). Hence, Gd is probably bound within the amorphous matrix surrounding the CFA nanocrystals. The local Gd structure, as revealed by EXAFS, can be described as a defective FAp-type bonding environment.

A similar conclusion was reached for Y,[34] while Ce is sequestered as a polynuclear Ce(III)–phosphate precipitate, also within the amorphous matrix.[33] Ce is 7-fold coordinated and forms CeO_7–PO_4–CeO_7 coordinated structures with d(Ce–Ce) = 4.97 Å (CeO_5–O_2–PO–O–CeO_6 linkage) (Fig. 7a). In contrast, Gd and Y are 8-fold coordinated and form Gd/YO_8–PO_4 and Gd/YO_8–CaO_6 coordinated structures with d(Gd–Ca) = 4.07–4.08 Å and d(Y–Ca) = 4.10 Å (Gd/YO_7–O–CaO_5 linkage) (Fig. 7b).[34] Cerium also precipitates in igneous rocks, forming monazite,[64] a 9-fold coordinated phosphate mineral ($^9CePO_4$).[59] While REY(PO_4) polymorphs of monazite do not occur naturally, they can be synthesized. Nucleation of REY(PO_4) requires free REY to be in excess of its solid solubility at a given phosphate concentration. The solubility constant of Ce for the reaction $REY(PO_4)_{(s)} \rightarrow REY^{3+} + PO_4^{3-}$ is $10^{-26.3}$, while those of Gd and Y are $10^{-25.6}$ and $10^{-25.02}$, respectively.[65] Therefore, Ce is 5 times less soluble than Gd and 19 times less than Y. The higher solubility of REY(PO_4) compounds compared to monazite[66]

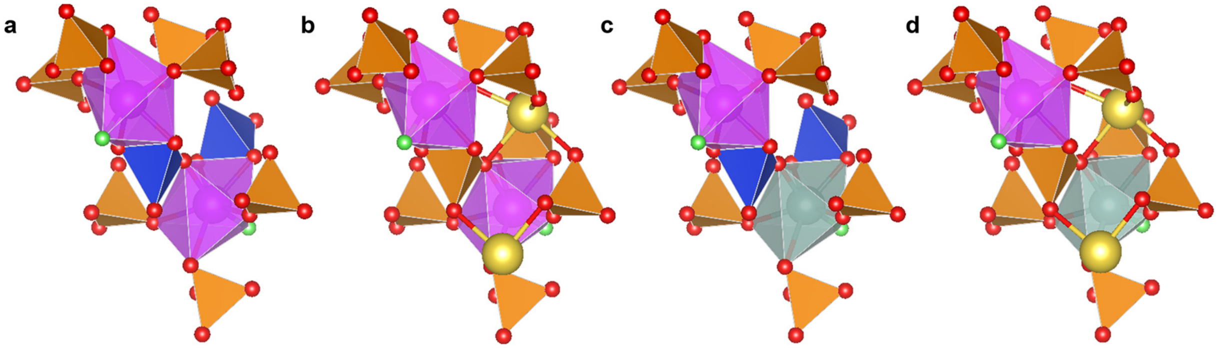

Fig. 6 Polyhedral representation of the local structure of Gd and Y as obtained by p-DFT. a) Gd–Gd model with Si for P charge compensation. b) Gd–Gd model with Na(1) for Ca(1) charge compensation. c) Gd–Y model with Si for P charge compensation. d) Gd–Y model with Na(1) for Ca(1) charge compensation. Gd(2) site, purple; Y(2) site, light green; Na, yellow; P, light brown; Si, blue; O, red; F, light green.

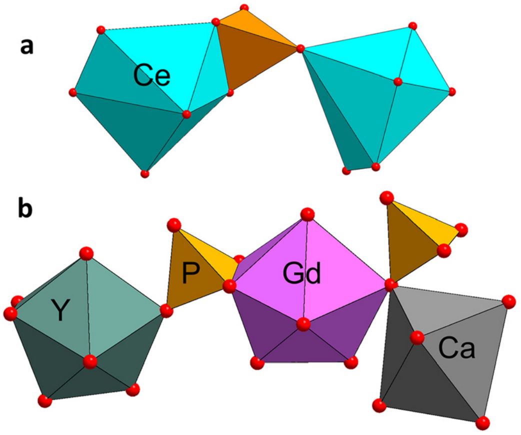

Fig. 7 Coordination of the CeO_7 (a) and GdO_8 (b) polyhedra in CFA. Ce, cyan; Gd, purple; Y, light green; P, light brown; O, red.

leads to the incorporation of REY into the monazite structure rather than their precipitation as pure phosphate minerals in nature. In bioapatite, Ce also precipitates as a Ce–phosphate phase,[33] but there is no evidence of Gd and Y in it. Instead, the two REY are incorporated into a calcium–phosphate matrix and are likely segregated, as predicted by p-DFT calculations (Fig. 6). Kato *et al.*[11] found that over 90% of REY could be extracted from sediment mud with dilute acids, while only 30% of Ce was recovered. The high leachability of REY is likely due to their presence in a defective Ca–phosphate phase, since poorly ordered atomic structures tend to be less stable than crystalline forms, and FAp is weakly soluble.[30,31] The lower recovery of Ce is attributed to its incorporation into a less soluble Ce–phosphate phase.

The energetically favorable Gd–Gd and Gd–Y pairs in FAp have d(Gd–Gd,Y) = 6.1–6.3 Å and GdO_4–O_2–P/SiO–O–Gd/YO_5 linkage. In the ^{8}Gd-phosphate and ^{8}Y-phosphate structures from the ICSD, the distances between two GdO_8 polyhedra and two YO_8 polyhedra connected by a PO_4 group range from 5.18 to 6.45 Å, and they increase with the REY–O–O–REY dihedral angle (Fig. 8). As a result, the REY–REY distances are likely broadly distributed at medium-range distances within the amorphous biogenic CFA matrix, since the polyhedral configuration of the polynuclear Gd/Y–phosphate clusters is more flexible in a disordered medium than in a crystalline structure. The widespread variation in Gd–Gd/Y distances, along with their long metrics, further complicates the detection of the Gd–Gd/Y pairs using EXAFS spectroscopy. The polyhedral structure of GdO_8 in the amorphous matrix of biogenic CFA is illustrated in Fig. 7b.

This research illustrates the unique capabilities of a high-luminosity wavelength-dispersive spectrometer to measure the EXAFS spectra of trace elements free of parasitic fluorescence peaks from the other elements in the matrix. Combined with atomistic calculations, HERFD-EXAFS can provide a comprehensive understanding of the molecular-scale mechanisms governing metal transport and retention in environmental and engineered systems.

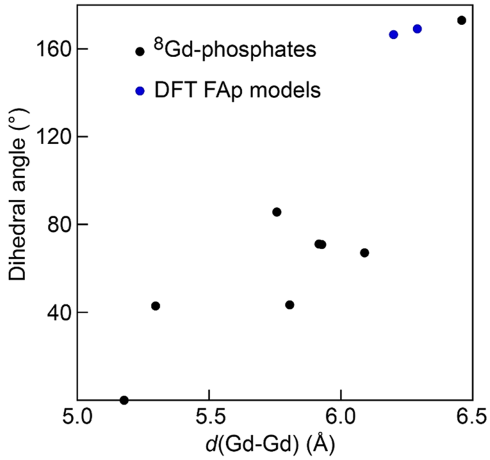

Fig. 8 Relationship between the Gd–Gd distance in GdO_8–PO_4–GdO_8 coordination structures and the Gd–O–O–Gd dihedral angle. The PO_4 tetrahedra are connected through their apices to the GdO_8 polyhedra (*i.e.*, corner linkage), unless otherwise noted. Black dots: crystal structures from the ICSD.[54–58] Blue dots: Gd2Y2_62_Si_ECT_E_48 and Gd2Y2_63_2Na1_55 DFT models from Fig. S5. PO_4 is replaced with SiO_4 in the Gd2Y2_62_Si_ECT_E_48 model.

4. Materials and methods

4.1. Natural CFA and FAp

The two b-CFA samples (16GC-194, 16GC-470) were collected during the RV SONNE cruise SO268.[67] Their mineralogy and geochemistry have been characterized previously.[33] Micrometric fish bones and teeth were carefully hand-picked under a binocular microscope and placed on a carbon adhesive tab for HERFD-EXAFS measurement. The magmatic fluorapatite (m-FAp) reference consists of a single crystal from Imilchil, Morocco, containing 385 mg Gd per kg (ppm).[68]

4.2. HR-TEM

The high-resolution transmission electron microscopy image of Fig. 1 was obtained using a Themis Z G3 Cs-probe corrected microscope (Thermo Fisher Scientific) equipped with a GATAN 4K OneView camera (resolution ~1.8 Å) operated at 300 kV. A thin lamella of the sample was prepared using a Zeiss crossbeam 550L focused ion beam – scanning electron microscope (FIB-SEM).

4.3. REY-sorbed HAp

All chemicals used were of analytical grade or higher and obtained from Sigma-Aldrich. Our previous study on Y[34] showed that Y(III)–carbonate complexation in solution does not alter the structure of the Y(III) surface complex on HAp. Given the similar ionic characteristics of Gd(III) and Y(III), Gd(III) sorption experiments were conducted under atmospheric conditions. The pH was kept at 7.5 due to the low solubility of Gd(III) at seawater pH (~8) in the presence of atmospheric carbonates (Fig. S7), alongside with the increased HAp dissolution below pH 7.[69] The HAp suspension was prepared as detailed previously,[34] but without $NaHCO_3$. Gd-HAp was synthesized by adding 7.5 mL of 857 μM $GdCl_3$ stock solution to a HAp suspension that was pre-equilibrated and maintained at pH 7.5 (905 Titrando, Metrohm). Because b-CFA has approximately 10 times more Y atoms than Gd atoms,[21] the influence of Y on Gd sorption was examined by adding 3.75 mL of 857 μM $GdCl_3$ ($3.21\ 10^{-6}$ moles) and 32.1 mL of 872 μM YCl_3 ($28.0\ 10^{-6}$ moles) into a separate HAp suspension (Gd,Y-HAp). The Gd/Y weight ratio resulted in 1000 mg kg^{-1}/5100 mg kg^{-1}. Both sorption samples were aged for 7 days at a final volume of approximately 480 mL. Less than 50 mL of 0.01 M NaOH was added to maintain the pH during the equilibration period. After 7 days, the solids were collected and lyophilized for 2 days until reaching constant weight, then stored at −80 °C.

The concentrations of Gd and Y in Gd-HAp and Gd,Y-HAp were measured using inductively coupled plasma mass spectrometry (ICP-MS 7900, Agilent, ISTerre, University of Grenoble-Alpes). The solids were fully digested in a HNO_3–HF mixture (volume ratio 3 : 4) at 185 °C for 2 h. After evaporation, the residues were dissolved in 2% HNO_3 (v/v), filtered through a 0.22 μm PES membrane (Carl ROTH), and analyzed. The measured concentrations were 2105 mg Gd per kg for Gd-HAp, and 1053 mg Gd per kg and 5184 mg Y per kg for Gd,Y-HAp.

4.4. Synthesis of $GdPO_4·H_2O$

The reference was prepared by adding 300 mL of 0.05 M $GdCl_3$ to a vessel containing 60 mL of 1 M H_3PO_4 while continuously stirring.[61] Several volumes of 8 M NaOH were added until the solution became turbid. The suspension was maintained for three days. The solid was rinsed and lyophilized to a constant weight. X-ray diffraction (Fig. S8, ID22, ESRF)[70] showed that the as-synthesized compound is poorly crystallized,[71] while EXAFS showed that it is well ordered at the local scale.

4.5. HERFD-EXAFS spectroscopy

The Gd L_3-edge HERFD-EXAFS spectra of the natural samples (16GC-194, 16GC-470, m-FAp) were collected at station I20-scanning of the Diamond Light Source (United Kingdom).[72] The X-ray beam was monochromatized using a Si(111) crystal 4-bounce monochromator[73] with a spot size of approximately 1 × 1 mm². The Yb $L_{\alpha1}$ ($3d_{5/2} \rightarrow 2p_{3/2}$) photoemission line was selected using the Si(333) reflection of 14 spherical analyzer crystals set at a Bragg angle of 78.49° in a vertical Rowland geometry. The diffracted intensity was measured with a Si drift detector (SDD). Multiple EXAFS spectra were acquired in *k*-step mode for 10–16 min, with a counting time of 1 second per point before the edge and from 2 seconds per point to 10 seconds per point after the edge. It took between 16 h and 24 h per sample to obtain quality data. All measurements were performed at 5–6 K, and no changes in spectral features indicating radiation damage were noted during the data collection. The multiple scans were averaged and reduced with the Athena software,[74] and fitted with WinXAS.[75] Theoretical amplitude and phase shift functions for the Gd–O, Gd–P, and Gd–Ca pairs were generated using FEFF 8.2 (ref. 76) with the Gd–FAp DFT model from Dahbi *et al.*[45] The Gd–Y functions were calculated by replacing Ca with Y in the Gd–FAp model.

4.6. Conventional EXAFS spectroscopy

The Gd L_3-edge EXAFS spectra of the references ($GdPO_4·H_2O$, Gd-HAp, Gd,Y-HAp) were collected at room temperature on beamline BM23 at the European Synchrotron Radiation Facility (ESRF). Data were collected on pressed pellets in fluorescence-yield mode with a Vortex®-ME7 silicon drift detector (Hitachi, Japan). $GdPO_4·H_2O$ was diluted in cellulose to prevent overabsorption. Several scans of 10 min were acquired in continuous scan mode with a 1 eV step and averaged. Data were processed similarly to those from the natural samples.

4.7. DFT

np-DFT calculations were performed using ORCA[77] and p-DFT using the Vienna *ab initio* simulation package (VASP),[78,79] as described previously in our Ce[45] and Y[34] studies. ORCA and VASP calculations were conducted at the GGA theory level using the Perdew–Burke–Ernzerhof (PBE)[80] density functional. The generalized gradient approximation GGA theory level was preferred over more demanding hybrid functional approximations,[51,81,82] as they predict similar atomic distances to X-ray diffraction ($\langle d(\text{P–O})\rangle^{\text{VASP}}_{\text{GGA}}$ = 1.516 Å, $\langle d(\text{P–O})\rangle^{\text{VASP}}_{\text{B3LYP}}$ = 1.547 Å, $\langle d(\text{P–O})\rangle_{\text{XRD}}$ = 1.535 Å).[83] Furthermore, the cell required for moderately enriched (<2%) structures ($GdCcCa_{79}(PO_4)_{48}F_{16}$ in eqn (1) and (2)) is prohibitively big for Hartree–Fock-based methods. The plane-wave cutoff energy for VASP was set to 500 eV, and weak interactions were included using the density-dependent dispersion correction (dDsC).[84,85] The electronic wavefunctions in the VASP were converged to 10^{-6} eV, while the geometry optimizations ended when all forces were below 0.05 eV $Å^{-1}$. All periodic structures used 2 × 2 × 2 bulk supercells. The supercells were prepared by replacing Ca(2) with Gd or Y, or both, and balancing the charges by substituting a silicate group for a phosphate group, or a Na^+ for a Ca^{2+} ion.

Author contributions

A. M: conceptualization, funding acquisition, methodology, formal analysis, writing – original draft. A. G.: methodology, formal analysis, writing – review and editing. A.-C. G.: methodology, formal analysis. Y. L., J. L., L. S., A. S.: methodology. A. K., O. M.: conceptualization, methodology. S. N. S.: conceptualization, funding acquisition, methodology, formal analysis, writing – review and editing.

Conflicts of interest

There are no conflicts to declare.

Data availability

The data supporting this article have been included as part of the supplementary information (SI).

Supplementary information: SI tables, and figures, input scripts for DFT2FEFFIT, Cartesian coordinates of the p-DFT models used in DFT2FEFFIT, EXAFS spectra (PDF). DFT-optimized geometries and associated README files (ZIP). All p-DFT computations are available under https://doi.org/10.17172/NOMAD/2025.11.04-2. See DOI: https://doi.org/10.1039/d5en01056j.

Acknowledgements

Sophie A. L. Paul is acknowledged for providing the biogenic apatites, Catherine Dejoie for measuring the XRD pattern of $GdPO_4 \cdot H_2O$, Célia Ragon for the FIB preparation, and Eric Gautron for access to the Nant'Themis TEM of the IMN's characterization platform PLASSMAT. Computational resources were provided by the "Centre Blaise Pascal de simulation et modélisation numérique (CBPSMN)", which runs with the SIDUS solution.[86] The authors wish to thank the Diamond Light Source for the award of beam time (proposal SP34350-1), and Dr. Matteo Aramini for his help during measurements. Financial support was provided by the European Union (ERC, Advanced Grant DEEP-SEE, 101052913). The views and opinions expressed are solely those of the authors and do not necessarily reflect those of the European Union or the European Research Council Executive Agency. The European Union and the granting authority accept no responsibility for the views expressed herein.

References

1 P. Caravan, J. J. Ellison, T. J. McMurry and R. B. Lauffer, Gadolinium(III) chelates as MRI contrast agents: Structure, dynamics, and applications, *Chem. Rev.*, 1999, **99**, 2293–2352.
2 A. Smith, C. R. H. Bahl, R. Bjork, K. Engelbrecht, K. K. Nielsen and N. Pryds, Materials Challenges for High Performance Magnetocaloric Refrigeration Devices, *Adv. Energy Mater.*, 2012, **2**, 1288–1318.
3 J. Dumazert, R. Coulon, Q. Lecomte, G. H. V. Bertrand and M. Hamel, Gadolinium for neutron detection in current nuclear instrumentation research: A review, *Nucl. Instrum. Methods Phys. Res., Sect. A*, 2018, **882**, 53–68.
4 T. Piotrowski, Neutron shielding evaluation of concretes and mortars: A review, *Constr. Build. Mater.*, 2021, **277**, 122238.
5 K. B. Wang, L. T. Ma, C. Yang, Z. Y. Bian, D. D. Zhang, S. Cui, M. L. Wang, Z. Chen and X. F. Li, Recent Progress in Gd-Containing Materials for Neutron Shielding Applications: A Review, *Materials*, 2023, **16**, 4305.
6 C. Xu, J. Kynicky, M. P. Smith, A. Kopriva, M. Brtnicky, T. Urubek, Y. Yang, Z. Zhao, C. He and S. Wenlei, Origin of heavy rare earth mineralization in South China, *Nat. Commun.*, 2017, **8**, 14598.
7 G. A. Moldoveanu and G. V. Papangelakis, An overview of rare-earth recovery by ion-exchange leaching from ion-adsorption clays of various origins, *Mineral. Mag.*, 2016, **80**, 63–76.
8 A. M. Borst, M. P. Smith, A. A. Finch, G. Estrade, C. Villanova-de-Benavent, P. Nason, E. Marquis, N. J. Horsburgh, K. M. Goodenough, C. Xu, J. Kynicky and K. Geraki, Adsorption of rare earth elements in regolith-hosted clay deposits, *Nat. Commun.*, 2020, **11**, 4386.
9 K. M. Goodenough, F. Wall and D. Merriman, The Rare Earth Elements: Demand, Global Resources, and Challenges for Resourcing Future Generations, *Nat. Resour. Res.*, 2018, **27**, 201–216.
10 G. F. Wang, J. X. Zhu, X. L. Liang, B. W. Ling, J. Xu, Y. Q. Yang, S. C. Kang, W. Tan, Y. J. Xu, X. S. Zou, L. Y. Ran, J. M. Wei and H. P. He, Industrial-scale sustainable rare earth mining enabled by electrokinetics, *Nat. Sustain.*, 2025, **8**, 182–189.
11 Y. Kato, K. Fujinaga, K. Nakamura, Y. Takaya, K. Kitamura, J. Ohta, R. Toda, T. Nakashima and H. Iwamori, Deep-sea mud in the Pacific Ocean as a potential resource for rare-earth elements, *Nat. Geosci.*, 2011, **4**, 535–539.
12 Y. Takaya, K. Yasukawa, T. Kawasaki, K. Fujinaga, J. Ohta, Y. Usui, K. Nakamura, J. I. Kimura, Q. Chang, M. Hamada, G. Dodbiba, T. Nozaki, K. Iijima, T. Morisawa, T. Kuwahara, Y. Ishida, T. Ichimura, M. Kitazume, T. Fujita and Y. Kato, The tremendous potential of deep-sea mud as a source of rare-earth elements, *Sci. Rep.*, 2018, **8**, 5763.
13 D. Bi, X. Shi, M. Huang, M. Yu, T. Zhou, Y. Zhang, A. Zhu, M. Shi and X. Fang, Geochemical and mineralogical characteristics of deep-sea sediments from the western North Pacific Ocean: Constraints on the enrichment processes of rare earth elements, *Ore Geol. Rev.*, 2021, **138**, 104318.
14 T. C. Zhou, X. F. Shi, M. Huang, M. Yu, D. J. Bi, X. W. Ren, J. H. Liu, A. M. Zhu, X. S. Fang and M. U. Shi, Genesis of REY-rich deep-sea sediments in the Tiki Basin, eastern South Pacific Ocean: Evidence from geochemistry, mineralogy and isotope systematics, *Ore Geol. Rev.*, 2021, **138**, 104330.
15 T. C. Zhou, X. F. Shi, M. Huang, M. Yu, D. J. Bi, X. W. Ren, G. Yang and A. M. Zhu, The Influence of Hydrothermal Fluids on the REY-Rich Deep-Sea Sediments in the Yupanqui Basin, Eastern South Pacific Ocean: Constraints from Bulk Sediment Geochemistry and Mineralogical Characteristics, *Minerals*, 2020, **10**, 1141.
16 J. Ohta, K. Yasukawa, S. Machida, K. Fujinaga, K. Nakamura, Y. Takaya, K. Iijima, K. Suzuki and Y. Kato, Geological factors responsible for REY-rich mud in the western North Pacific Ocean: Implications from mineralogy and grain size distributions, *Geochem. J.*, 2016, **50**, 591–603.
17 J. L. Liao, X. M. Sun, D. F. Li, R. N. Sa, Y. Lu, Z. Lin, L. Xu, R. Z. Zhan, Y. G. Pan and H. F. Xu, New insights into nanostructure and geochemistry of bioapatite in REE-rich deep-sea sediments: LA-ICP-MS, TEM, and Z-contrast imaging studies, *Chem. Geol.*, 2019, **512**, 58–68.
18 J. L. Liao, J. Y. Chen, X. M. Sun, Z. W. Wu, Y. A. Deng, X. F. Shi, Y. J. Y. Wang, Y. Chen and A. Koschinsky, Quantifying the controlling mineral phases of rare-earth elements in deep-sea pelagic sediments, *Chem. Geol.*, 2022, **595**, 120792.

19 Y. Kon, M. Hoshino, K. Sanematsu, S. Morita, M. Tsunematsu, N. Okamoto, N. Yano, M. Tanaka and T. Takagi, Geochemical characteristics of apatite in heavy REE-rich deep-sea mud from Minami-Torishima area, Southeastern Japan, *Resour. Geol.*, 2014, **64**, 47–57.

20 T. Kashiwabara, R. Toda, K. Nakamura, K. Yasukawa, K. Fujinaga, S. Kubo, T. Nozaki, Y. Takahashi, K. Suzuki and Y. Kato, Synchrotron X-ray spectroscopic perspective on the formation mechanism of REY-rich muds in the Pacific Ocean, *Geochim. Cosmochim. Acta*, 2018, **240**, 274–292.

21 A. Manceau, S. Paul, A. Simionovici, V. Magnin, M. Balvay, N. Findling, M. Rovezzi, S. Muller, D. Garbe-Schonberg and A. Koschinsky, Fossil Bioapatites with Extremely High Concentrations of Rare Earth Elements and Yttrium from Deep-Sea Pelagic Sediments, *ACS Earth Space Chem.*, 2022, **6**, 2093–2103.

22 J. Liao, J. Chen, X. Sun, Y. Deng, Y. Wang, D. Wang, G. Hong, L. Klose and A. Koschinsky, Controlling Factors on REY Enrichments in Basins From the Pacific Ocean: Early Diagenesis and Local Constraints, *Geochem., Geophys., Geosyst.*, 2024, **25**, e2023GC01111.

23 W. X. Fan, J. M. Zhou, X. D. Jiang, H. Zhang, M. Mi, P. Yuan, Y. H. Dong, D. Liu, Y. F. Wei and J. Peckmann, Carbonate fluorapatite coatings on phillipsite represent a significant sink of phosphorus in abyssal plains of the western Pacific Ocean, *Proc. Natl. Acad. Sci. U. S. A.*, 2025, **122**, e2407683122.

24 K. C. Ruttenberg and R. A. Berner, Authigenic apatite formation and burial in sediments from non-upwelling, continental margin environments, *Geochim. Cosmochim. Acta*, 1993, **57**, 991–1007.

25 J. Liao, D. Wang, X. M. Sun, G. Hong, Y. Deng, W. Yao, A. Manceau and A. Koschinsky, Carbonate fluorapatite pellets in pelagic sediments: Implications for REY enrichment and Nd isotopic signatures in abyssal environments, *Earth Planet. Sci. Lett.*, 2025, **671**, 119658.

26 T. Kashiwabara, R. Toda, K. Fujinaga, T. Honma, Y. Takahashi and Y. Kato, Determination of host phase of lanthanum in deep-sea REY-rich mud by XAFS and μ-XRF using high-energy synchrotron radiation, *Chem. Lett.*, 2014, **43**, 199–200.

27 K. Yasukawa, H. Liu, K. Fujinaga, S. Machida, S. Haraguchi, T. Ishii, K. Nakamura and Y. Kato, Geochemistry and mineralogy of REY-rich mud in the eastern Indian Ocean, *J. Asian Earth Sci.*, 2014, **93**, 25–36.

28 R. N. Sa, X. M. Sun, G. W. He, L. Xu, Q. Q. Pan, J. L. Liao, K. C. Zhu and X. G. Deng, Enrichment of rare earth elements in siliceous sediments under slow deposition: A case study of the central North Pacific, *Ore Geol. Rev.*, 2018, **94**, 12–23.

29 Y. Chen, H. Zhang, Y. Dong, T. Wang, W. Zhang, J. Lu, Z. Zhu, X. Li and F. Chu, In-situ geochemistry of fish teeth in REE-rich mud: Indicating Missing REE-Bearing Mineral Phases for Mass Balance, *Ore Geol. Rev.*, 2025, **184**, 106746.

30 F. Berna, A. Matthews and S. Weiner, Solubilities of bone mineral from archaeological sites: the recrystallization window, *J. Archaeol. Sci.*, 2004, **31**, 867–882.

31 A. Antignano and C. E. Manning, Fluorapatite solubility in H_2O and H_2O–NaCl at 700 to 900 °C and 0.7 to 2.0 GPa, *Chem. Geol.*, 2008, **251**, 112–119.

32 C. Chaïrat, J. Schott, E. H. Oelkers, J. E. Lartigue and N. Harouiya, Kinetics and mechanism of natural fluorapatite dissolution at 25 °C and pH from 3 to 12, *Geochim. Cosmochim. Acta*, 2007, **71**, 5901–5912.

33 A. Manceau, A.-C. Gaillot, J. Liao, Y. Li, O. Mathon, K. A. Lomachenko, P. Glatzel, A. Simionovici, M. Balvay, S. A. L. Paul, A. Koschinsky and S. N. Steinmann, Cerium occurs as cerium-phosphate clusters around bioapatite nanocrystals in deep-sea sediments, *Commun. Earth Environ.*, 2025, **6**, 466.

34 A. Manceau, Y. Li, A. Giacomelli, A.-C. Gaillot, J. L. Liao, V. Magnin, L. Spadini, Y. Deng, A. Koschinsky, O. Mathon and S. N. Steinmann, Structural Form of Yttrium in Nanocrystalline Fluorapatite from Marine Sediments at 0.11 Å Resolution, *Chem. Mater.*, 2025, **37**, 7939–7951.

35 M. Ondrejka, P. Uher, S. Ferenc, J. Majzlan, K. Pollok, T. Mikus, S. Milovská, A. Molnárová, R. Skoda, R. Kopácik, S. Kurylo and P. Bacik, Monazite-(Gd), a new Gd-dominant mineral of the monazite group from the Zimna Voda REE-U-Au quartz vein, Prakovce, Western Carpathians, Slovakia, *Mineral. Mag.*, 2023, **87**, 568–574.

36 P. Glatzel, T. C. Weng, K. Kvashnina, J. Swarbrick, M. Sikora, E. Gallo, N. Smolentsev and R. A. Mori, Reflections on hard X-ray photon-in/photon-out spectroscopy for electronic structure studies, *J. Electron Spectrosc. Relat. Phenom.*, 2013, **188**, 17–25.

37 M. Merkulova, O. Mathon, P. Glatzel, V. Batanova, P. Marion, M. C. Boiron and A. Manceau, Revealing the chemical form of 'invisible' gold in natural arsenian pyrite and arsenopyrite with high energy-resolution X-ray absorption spectroscopy, *ACS Earth Space Chem.*, 2019, **3**, 1905–1914.

38 A. Manceau, M. Merkulova, O. Mathon, P. Glatzel, M. Murdzek, V. Batanova, A. Simionovici, S. N. Steinmann and D. Paktunc, The mode of incorporation of As(-I) and Se(-I) in natural pyrite revisited, *ACS Earth Space Chem.*, 2020, **4**, 379–390.

39 C. Laskar, E. F. Bazarkina, M. A. Kokh, L. Hazemann, S. Foulon, O. Leynaud, E. Desmaele and G. S. Pokrovski, Exploring Platinum Speciation with X-ray Absorption Spectroscopy under High-Energy Resolution Fluorescence Detection Mode, *Minerals*, 2022, **12**, 1602.

40 G. S. Pokrovski, E. Desmaele, C. Laskar, E. F. Bazarkina, D. Testemale, J. L. Hazemann, R. Vuilleumier, A. P. Seitsonen, G. Ferlat and A. M. Saitta, Gold speciation in hydrothermal fluids revealed by in situ high energy resolution X-ray absorption spectroscopy, *Am. Mineral.*, 2022, **107**, 369–376.

41 O. N. Filimonova, B. R. Tagirov, A. L. Trigub, M. S. Nickolsky, M. Rovezzi, E. V. Belogub, V. L. Reukov and I. V. Vikentyev, The state of Au and As in pyrite studied by X-ray absorption spectroscopy of natural minerals and synthetic phases, *Ore Geol. Rev.*, 2020, **121**, 103475.

42 G. S. Pokrovski, M. A. Kokha, O. Proux, J. L. Hazemann, E. F. Bazarkina, D. Testemale, C. Escoda, M. C. Boiron, M. Blanchard, T. Aigouya, S. Gouya, P. de Perseval and M. Thibauta, The nature and partitioning of invisible gold in the pyrite-fluid system, *Ore Geol. Rev.*, 2019, **109**, 545–563.

43 T. Lender, G. Murphy, E. Bazarkina, A. Bukaemskiy, S. Gilson, M. Henkes, C. Hennig, A. Kaspor, J. Marquardt, J. Niessen, L. Peters, J. Poonoosamy, A. Rossberg, V. Svitlyk, K. O. Kvashnina and N. Huittinen, Investigation of Radiation Damage in the Monazite-Type Solid Solution $La_{1-x}Ce_xPO_4$, *Inorg. Chem.*, 2024, **63**, 17525–17535.

44 A. Manceau, R. Brossier, O. Mathon, K. A. Lomachenko, M. Retegan, P. Glatzel and S. N. Steinmann, DFT2FEFFIT: a density-functional-theory-based structural toolkit to analyze EXAFS spectra, *J. Appl. Crystallogr.*, 2024, **57**, 1229–1234.

45 S. Dahbi, A. Rosa, A. Manceau and S. N. Steinmann, Prediction and Rationalization of Site Preference of Rare Earth Elements in Fluorapatite from Density Functional Theory, *ACS Earth Space Chem.*, 2025, **9**, 1633–1641.

46 S. J. George, S. M. Webb, J. L. Abraham and S. P. Cramer, Synchrotron X-ray analyses demonstrate phosphate-bound gadolinium in skin in nephrogenic systemic fibrosis, *Br. J. Dermatol.*, 2010, **163**, 1077–1081.

47 J. M. Hughes, M. Cameron and K. D. Crowley, Structural variations in natural F, OH, and Cl apatites, *Am. Mineral.*, 1989, **74**, 870–876.

48 B. K. Teo, *EXAFS: basic principles and data analysis*, Springer-Verlag, Berlin, 1986.

49 J. H. Robblee, J. Messinger, R. M. Cinco, K. L. McFarlane, C. Fernandez, S. A. Pizarro, K. Sauer and V. K. Yachandra, The Mn cluster in the S_0 state of the oxygen-evolving complex of photosystem II studied by EXAFS spectroscopy:: Are there three di-μ-oxo-bridged Mn_2 moieties in the tetranuclear Mn complex?, *J. Am. Chem. Soc.*, 2002, **124**, 7459–7471.

50 H. Höppe and S. J. Sedlmaier, Crystal structures of incommensurately modulated $Ln(PO_3)_3$ (Ln = Tb-Yb) and commensurate $Gd(PO_3)_3$ and $Lu(PO_3)_3$, *Inorg. Chem.*, 2007, **46**, 3467–3474.

51 M. Corno, C. Busco, V. Bolis, S. Tosoni and P. Ugliengo, Water Adsorption on the Stoichiometric (001) and (010) Surfaces of Hydroxyapatite: A Periodic B3LYP Study, *Langmuir*, 2009, **25**, 2188–2198.

52 C. Park, P. Fenter, Z. Zhang, L. Cheng and N. C. Sturchio, Structure of the fluorapatite (100)-water interface by high-resolution X-ray reflectivity, *Am. Mineral.*, 2004, **89**, 1647–1654.

53 M. Fleet, X. Liu and Y. Pan, Site preference of rare earth elements in hydroxyapatite $[Ca_{10}(PO_4)_6(OH)_2]$, *J. Solid State Chem.*, 2000, **149**, 391–398.

54 F. Chehimi-Moumen, D. Ben Hassen-Chehimi, M. Ferid and M. Trabelsi-Ayadi, Preparation and structure of $HGdP_2O_7 \cdot 3H_2O$, *Mater. Res. Bull.*, 2001, **36**, 365–373.

55 G. M. Wolten, Structure of the M'-phase of $YTaO_4$, a third fergusonite polymorph, *Acta Crystallogr.*, 1967, **23**, 939–944.

56 A. J. Cramer and J. M. Cole, Host-guest prospects of neodymium and gadolinium ultraphosphate frameworks for nuclear waste storage: Multi-temperature topological analysis of nanoporous cages in RP_5O_{14}, *J. Solid State Chem.*, 2018, **266**, 250–257.

57 H. Ettis, H. Naïli and T. Mhiri, Reinvestigation of the GdP_5O_{14} crystal structure at room temperature and magnetic properties, *Mater. Chem. Phys.*, 2007, **102**, 275–280.

58 S. Rodriguez-Liviano, A. I. Becerro, D. Alcántara, V. Grazú, J. M. de la Fuente and M. Ocaña, Synthesis and Properties of Multifunctional Tetragonal Eu:$GdPO_4$ Nanocubes for Optical and Magnetic Resonance Imaging Applications, *Inorg. Chem.*, 2013, **52**, 647–654.

59 Y. Ni, J. M. Hughes and A. N. Mariano, Crystal chemistry of the monazite and xenotime structures, *Am. Mineral.*, 1995, **80**, 21–26.

60 A. Mbarek, M. Graia, G. Chadeyron, D. Zambon, J. Bouaziz and M. Fourati, Synthesis and crystal structure determination of yttrium ultraphosphate YP_5O_{14}, *J. Solid State Chem.*, 2009, **182**, 509–516.

61 M. R. Rafiuddin, C. Tyagi and M. A. Haq, Synthesis and structural investigation of churchite-type $REPO_4.2H_2O$ (RE = Y, Gd, Dy) nanocrystals, *J. Solid State Chem.*, 2022, **311**, 123150.

62 R. Essehli, B. El Bali, M. Dusek, K. Fejfarova and M. Lachkar, Yttrium hydrogendiphosphate trihydrate, *Acta Crystallogr., Sect. E: Struct. Rep. Online*, 2007, **63**, i80–i82.

63 D. F. Mullica, E. L. Sappenfield and L. A. Boatner, A structural investigation of several mixed lanthanide orthophosphates, *Inorg. Chim. Acta*, 1990, **174**, 155–159.

64 A. Chakhmouradian and F. Wall, Rare Earth Elements: Minerals, Mines, Magnets (and More), *Elements*, 2012, **8**, 333–340.

65 D. L. Parkhust and C. A. J. Appelo, Description of input and examples for PHREEQC version 3—A computer program for speciation, batch-reaction, one-dimensional transport, and inverse geochemical calculations, *U.S. Geological Survey Techniques and Methods*, 2013, vol. 6, p. 497.

66 A. Williams-Jones, A. Migdisov and I. Samson, Hydrothermal Mobilisation of the Rare Earth Elements – a Tale of 'Ceria' and 'Yttria', *Elements*, 2012, **8**, 355–360.

67 M. Haeckel and P. Linke, *RV SONNE Fahrtbericht/Cruise Report SO268 – Assessing the Impacts of Nodule Mining on the Deep-sea Environment: NoduleMonitoring, Manzanillo (Mexico) – Vancouver (Canada), 17.02.–27.05.2019*, 2021, p. 820.

68 A. Manceau, O. Mathon, K. A. Lomachenko, M. Rovezzi, K. O. Kvashnina, M. C. Boiron, R. Brossier and S. N. Steinmann, Revealing the incorporation of cerium in fluorapatite, *ACS Earth Space Chem.*, 2024, **8**, 119–128.

69 G. J. Levinskas and W. F. Neuman, The solubility of bone mineral. I. Solubility studies of synthetic hydroxylapatite, *J. Phys. Chem.*, 1955, **59**, 164–168.

70 A. Fitch, C. Dejoie, E. Covacci, G. Confalonieri, O. Grendal, L. Claustre, P. Guillou, J. Kieffer, W. de Nolf, S. Petitdemange, M. Ruat and Y. Watier, ID22-the high-resolution powder-diffraction beamline at ESRF, *J. Synchrotron Radiat.*, 2023, **30**, 1003–1012.

71 P. A. Lessing and A. W. Erickson, Synthesis and characterization of gadolinium phosphate neutron absorber, *J. Eur. Ceram. Soc.*, 2003, **23**, 3049–3057.

72 S. Diaz-Moreno, M. Amboage, M. Basham, R. Boada, N. E. Bricknell, G. Cibin, T. Cobb, J. Filik, A. Freeman, K. Geraki, D. Gianolio, S. Hayama, K. Ignatyev, L. Keenan, I. Mikulska, J. F. W. Mosselmans, J. Mudd and S. A. Parry, The Spectroscopy Village at Diamond Light Source, *J. Synchrotron Radiat.*, 2018, **25**, 998–1009.

73 S. Hayama, G. Duller, J. P. Sutter, M. Amboage, R. Boada, A. Freeman, L. Keenan, B. Nutter, L. Cahill, P. Leicester, B. Kemp, N. Rubies and S. Diaz-Moreno, The scanning four-bounce monochromator for beamline I20 at the Diamond Light Source, *J. Synchrotron Radiat.*, 2018, **25**, 1556–1564.

74 B. Ravel and M. Newville, ATHENA, ARTEMIS, HEPHAESTUS: data analysis for X-ray absorption spectroscopy using IFEFFIT, *J. Synchrotron Radiat.*, 2005, **12**, 537–541.

75 T. Ressler, WinXAS: a program for X-ray absorption spectroscopy data analysis under MS-Windows, *J. Synchrotron Radiat.*, 1998, **5**, 118–122.

76 A. L. Ankudinov and J. J. Rehr, Relativistic calculations of spin-dependent X-ray-absorption spectra, *Phys. Rev. B: Condens. Matter Mater. Phys.*, 1997, **56**, 1712–1716.

77 F. Neese, Software update: The ORCA program system-Version 5.0, *Wiley Interdiscip. Rev.: Comput. Mol. Sci.*, 2022, e1606.

78 G. Kresse, Ab-initio molecular-dynamics for liquid crystals, *J. Non-Cryst. Solids*, 1995, **193**, 222–229.

79 G. Kresse and J. Furthmuller, Efficiency of ab-initio total energy calculations for metals and semiconductors using a plane-wave basis set, *Comput. Mater. Sci.*, 1996, **6**, 15–50.

80 J. P. Perdew, K. Burke and M. Ernzerhof, Generalized gradient approximation made simple, *Phys. Rev. Lett.*, 1996, **77**, 3865–3868.

81 M. Corno, A. Rimola, V. Bolis and P. Ugliengo, Hydroxyapatite as a key biomaterial: quantum-mechanical simulation of its surfaces in interaction with biomolecules, *Phys. Chem. Chem. Phys.*, 2010, **12**, 6309–6329.

82 P. Canepa, F. Chiatti, M. Corno, Y. Sakhno, G. Martra and P. Ugliengo, Affinity of hydroxyapatite (001) and (010) surfaces to formic and alendronic acids: a quantum-mechanical and infrared study, *Phys. Chem. Chem. Phys.*, 2011, **13**, 1099–1111.

83 M. Corno, C. Busco, B. Civalleri and P. Ugliengo, Periodic ab initio study of structural and vibrational features of hexagonal hydroxyapatite $Ca_{10}(PO_4)_6(OH)_2$, *Phys. Chem. Chem. Phys.*, 2006, **8**, 2464–2472.

84 S. N. Steinmann and C. Corminboeuf, Comprehensive Benchmarking of a Density-Dependent Dispersion Correction, *J. Chem. Theory Comput.*, 2011, **7**, 3567–3577.

85 S. Gautier, S. N. Steinmann, C. Michel, P. Fleurat-Lessard and P. Sautet, Molecular adsorption at Pt(111). How accurate are DFT functionals?, *Phys. Chem. Chem. Phys.*, 2015, **17**, 28921–28930.

86 E. Quemener and M. Corvellec, SIDUS—the solution for extreme deduplication of an operating system, *Linux J.*, 2013, 235.